RESEARCH PAPER

Particle concentration via acoustically driven microcentrifugation: microPIV flow visualization and numerical modelling studies

Rohan V. Raghavan · James R. Friend · Leslie Y. Yeo

Abstract Through confocal-like microparticle image velocimetry experiments, we reconstruct, for the first time, the three-dimensional flow field structure of the azimuthal fluid recirculation in a sessile drop induced by asymmetric surface acoustic wave radiation, which, in previous two-dimensional planar studies, has been shown to be a powerful mechanism for driving inertial microcentrifugation for micromixing and particle concentration. Supported through finite element simulations, these insights into the three-dimensional flow field provide valuable information on the mechanisms by which particles suspended in the flow collect in a stack at a central position on the substrate at the bottom of the drop once they are convected by the fluid to the bottom region via a helical spiral-like trajectory around the drop periphery. Once close to the substrate, the inward radial velocity then forces the particles into this central stagnation point where they are trapped by sedimentary forces, provided the convective force is insufficient to redisperse them along with the fluid up a central column and into the bulk of the drop.

Keywords Surface acoustic waves ·
Particle concentration · Microfluidics ·
Microcentrifugation · Microparticle image velocimetry

1 Introduction

In the same way that unit operations constitute individual components in a macroscopic chemical processing plant,

R. V. Raghavan · J. R. Friend · L. Y. Yeo (✉)
Micro/Nanophysics Research Laboratory,
Department of Mechanical Engineering, Monash University,
133/31 Engineering, Clayton, VIC 3800, Australia
e-mail: leslie.yeo@eng.monash.edu.au

the lab-on-a-chip or microfluidic processor also comprises miniature versions of these units—micropumps, microreactors, microvalves, micromixers, and microseparators. Whilst considerable progress has been achieved through the past decade, challenges remain on two fronts: the miniaturization of the individual microfluidic components and their integration into practical biological and chemical analytical systems for applications in molecular analysis, biodefence and point-of-care diagnostics (Whitesides 2006).

Amongst these various microfluidic unit operations, microcentrifugation remains most primitive (Ducree 2008). Just like their macroscopic counterparts, microcentrifuges provide a powerful means for driving intense mixing or particle separation. The procedure is vital but yet time-consuming; for example, extraction of blood cells and other cellular components from blood plasma takes up to one-quarter of the entire processing time in clinical diagnostics to provide information to provide prognosis for disease. It is well known that simple tests on blood plasma can be used to evaluate the blood chemistry and the health of various organs in an individual (Blattert et al. 2004). Facilitating the extraction of blood cells, bacteria or other particulate matter from a sample at the scales required for lab-on-a-chip devices has proven to be difficult in the past. Conventional centrifugation and filtration techniques with microfilters (Sengupta and Chang 2008) and membranes are complex, cumbersome and complicated (Yuen et al. 2001; Brody et al. 1996; Wilding et al. 1994), requiring pumps to force the fluid through the filters. Besides the large size of the pumps, the act of forcing the fluid through small membrane pores is detrimental to the viability of biological cells, causing them to deform and denature during the process. Other techniques involving evaporation-based concentration (Walker and Beebe 2002) and

acoustic radiation pressure (Meng et al. 1999) have also been demonstrated as viable microfluidic concentration techniques. However, they again require complex setups which makes integrating them into a multi-purpose plat-forms a greater challenge.

A simpler approach has been the 'lab-on-a-CD' concept, wherein microfluidic components fabricated onto a compact disk are spun by exploiting Coriolis forces (Madou and Kellogg 1998). Rotation of the entire disk structure provides a non-specific acceleration to the entire micro-fluidic structure. This feature proves to be a cumbersome limitation since all components—whether upstream or downstream of the centrifuge area, including dispensing and sensor components—must be designed to operate over the entire range of accelerations. Whilst it may be possible to isolate merely the reactor and separator to the rotated disk, integration of the rotating component with stationary fixtures via microfluidic connections is at best complex and expensive.

More recently, Yeo et al. (2006a, b) and Arifin et al. (2007) have pioneered a novel microcentrifuge by driving an ionic wind, produced by applying a large gas phase electric field above a circular liquid microchamber. The bulk air flow then results in interfacial shearing of the liquid surface which drives bulk helical-like recirculation of the liquid in the microchamber. Over several minutes, such motion resulted in the separation of red blood cells from plasma. The use of large voltages—several kilo-volts—and the fairly slow concentration speed are draw-backs to this approach, though these issues are less of a problem than other technologies used for the purpose in the past.

Better yet, both the requirement for large voltages and the problem of slow concentration were circumvented through the use of leaky surface acoustic waves (SAWs) to drive the microcentrifugation. As with other SAW-driven microfluidic actuation (Yeo and Friend 2009), including vibration-induced particle patterning and sorting (Li et al.

2008), drop translation (Wixforth 2003; Tan et al. 2007b), jetting (Tan et al. 2009) and atomization (Friend et al. 2008; Qi et al. 2008; Alvarez et al. 2008a, b, 2009), the microcentrifugation driven by SAW is extremely fast (Li et al. 2007), especially with the use of elliptical transducers to focus the SAWs (Tan et al. 2007a; Shilton et al. 2008). The perceived difficulties of using lithium niobate in SAW microfluidics is in some part countered by using fluid coupling to microfluidic devices in other materials (Hodgson et al. 2009).

When subjected to asymmetrical SAW radiation, 5 μm particles seeded in a 30 μl drop are observed to concentrate rapidly in the center of the drop, as shown in Fig. 1. Li et al. (2007) attributed this phenomena to the competition between shear induced migration—arising due to azi-muthal velocity gradients within the drop which result in the transport of the particles across azimuthal streamlines into the interior of the vortex (see Fig. 1)—and acousti-cally-driven inertial convection within the drop—*acoustic streaming*—which acts to disperse the particles. Below a critical threshold value in the applied power, approxi-mately 300 mW, the shear diffusion process is dominant therefore leading to the concentration of the particles in the closed vortex. However, beyond this critical value, the acoustic streaming-driven convection dominates, giving rise to particle dispersion.

In Li et al. (2007) and Shilton et al. (2008), the particle concentration dynamics were quantified using a relatively simple two-dimensional horizontal plane pixel intensity analysis of the temporal variation in gray-scale video frames, omitting the particle dynamics in a direction per-pendicular to the plane. Whilst this provides a quantitative description of the dynamics sufficient to determine the underlying physical mechanisms, it ignores the effect of the three-dimensional flow field of the particle trajectory and hence also the concentration process. Past studies, includ-ing Yeo et al. (2006a, b) and Arifin et al. (2007), have been less affected by the three-dimensional nature of the flow
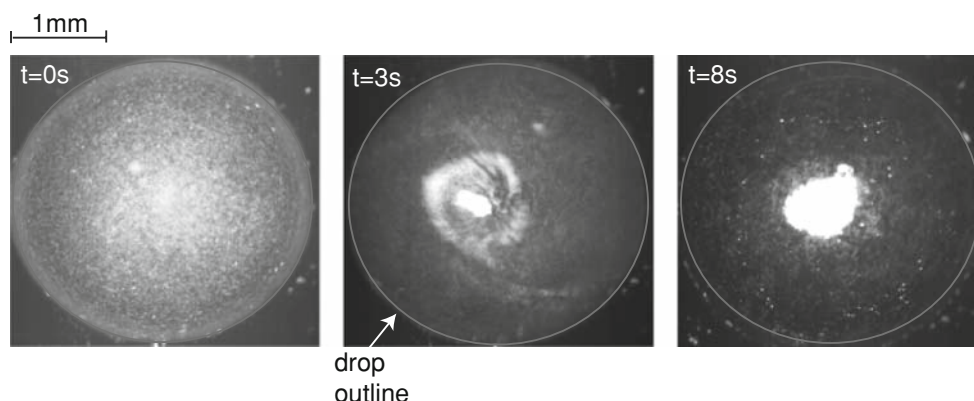

Fig. 1 Video images captured at 60 frames/s illustrating rapid particle concentration using asymmetric SAW radiation

field, yet even then these effects were found to be significant. With SAW-driven acoustic streaming in fluid drops, the flow field is certainly three-dimensional in nature and only poorly understood when confined to a drop. Having a fundamental understanding of the nature of the flow within the drop would shed light on the other SAW-driven drop microfluidic processes, including drop transport (Wixforth et al. 1990; Tan et al. 2007b), jetting (Tan et al. 2009) and atomization (Friend et al. 2008; Qi et al. 2008; Alvarez et al. 2008a, b; 2009).

In this work, we employ experimental visualization using microparticle image velocimetry (microPIV) (Papautsky et al. 2008) together with numerical simulations to provide a qualitative and quantitative understanding of the three-dimensional flow field and particle concentration dynamics. In Sect. 2, we provide a brief introduction to the SAW and how it drives microfluidic actuation as well as the experimental techniques employed to characterize the three-dimensional flow field within the drop. In Sect. 3, we discuss the numerical simulation used to examine the flow field induced by the SAW device. This is followed by the experimental and numerical results and their interpretation to construct a physical picture of the flow trajectories and the particle concentration within the drop. The final section then draws conclusions based on our findings.

2 Experimental setup

A SAW is a nanometer-order amplitude electroacoustic traveling wave that propagates on the surface of a piezoelectric crystal substrate, as shown in Fig. 2. When an electric field is applied across a piezoelectric material, it generates an elastic deformation via the converse piezoelectric effect. Single crystal lithum niobate (LN) is one of many such materials that is especially well-suited for use in SAW devices for microfluidic applications, due to its low acoustic attenuation and relatively large electromechanical coupling from a few MHz to several GHz. The necessary electric field is created with the help of metallic interdigital transducers (IDTs) that are deposited onto the surface of the crystals. When supplied with a sinusoidal electrical signal, the IDT produces a corresponding periodic strain pattern on the surface that results in a *Rayleigh wave* that propagates away from it. Rayleigh waves decay exponentially into the piezoelectric material, essentially confining the wave energy to within a few wavelengths (typically 5–6 wavelengths) from the surface. They have displacements both normal to the surface and along it, parallel to the wave propagation direction (White and Voltmer 1965); the displacements are temporally a quarter wavelength out of phase and are roughly the same amplitude. Because the frequency used in these SAW devices are at least a few
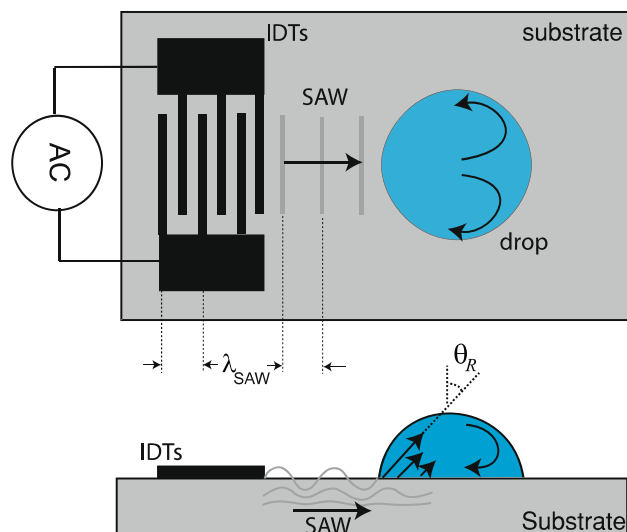
Fig. 2 Schematic illustrating the propagation of the SAW on a substrate and its interaction with a sessile fluid drop placed on the substrate. The top image is a plan view and the bottom image is the side view. Note the leakage of the SAW energy into the drop at the Rayleigh angle θ_R. The SAW has wavelength λ_{SAW}, which is set by the width and gap of the interdigital electrodes (IDTs)
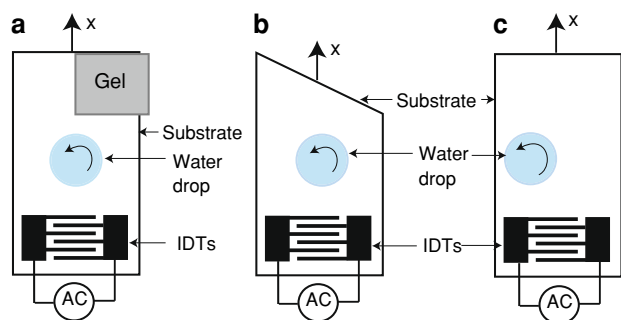
MHz, the acceleration of points along the surface in the piezoelectric substrate is several hundred million m/s^2. If a drop is placed on the substrate in the transmission path of the SAW, a portion of the longitudinal component of the wave is refracted into the fluid medium at an angle known as the Rayleigh angle $\theta_R = \sin^{-1}(c_l/c_s)$; c_l and c_s are the sound speeds in the liquid and substrate, respectively—for water, θ_R is therefore approximately 23°, defined from the vertical axis, as shown in Fig. 2. This refracted energy appears as a longitudinal sound wave in the fluid and is ultimately responsible for *acoustic streaming* (Wixforth 2003) once the wave has reached sufficient intensity to induce compressibility effects in the fluid. Given the tremendous accelerations induced by the SAW, compression in fluids typically considered "incompressible", like water, is straightforward.

By varying the electrical power applied to the IDTs, a parameter directly related to the amplitude of the SAW, three modes of fluid actuation may be excited. At low power, the drop vibrates with elastic motion of the free fluid surface and, at a given critical value, acoustic streaming within the drop commences (Li et al. 2008). Increasing the applied power further, the fluid drop itself will then move along the surface in the direction of SAW propagation due to a horizontal body force acting on the drop as a consequence of the longitudinal sound wave propagating into it at the Rayleigh angle (Tan et al. 2007b). At even higher powers, interfacial destabilization results in the atomization of the fluid from the drop's free surface leading to the ejection of a fine aerosol mist (Qi et al.

2008). In this study however, the power is limited to the amount required to induce acoustic streaming as neither fluid translation nor atomization is of interest.

To drive azimuthal recirculation and with it the particle concentration described earlier, an asymmetric distribution of SAW radiation needs to be supplied to the drop such that one-half of the drop receives more acoustic energy than the other. This can be achieved by a variety of symmetry-breaking means, as shown in Fig. 3; for example, by placing an absorbing gel to damp out the wave reflections from one half of the substrate's edge, introducing a diagonal cut to the SAW substrate to induce asymmetrical wave reflections at the substrate edges, or, by placing the drop such that a part of it resides outside the SAW propagation pathway (Li et al. 2007).
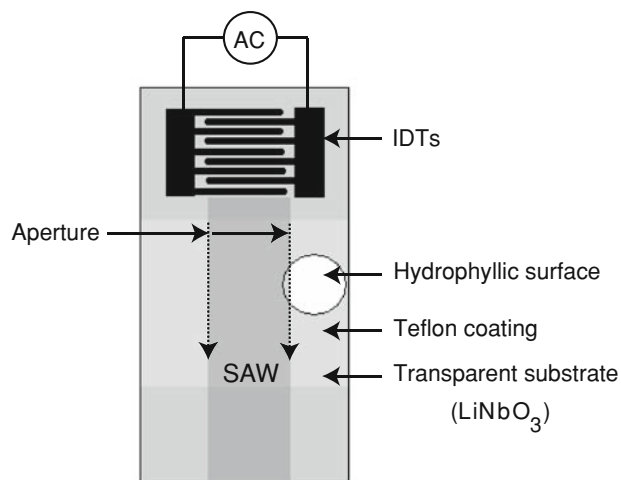
A device setup similar to that shown in Fig. 3c was employed here. The IDT was fabricated using standard UV photolithography in a basic full-width interleave configuration constructed from 300 nm thick aluminum atop a 20 nm thick chromium layer both sputter deposited onto a 127.68° Y-X cut, X-propagating lithium niobate (Roditi Ltd., London, UK) single-crystal piezoelectric substrate. The substrate was optically polished on both sides to render it transparent and allow the interior of the fluid drop to be observed from the distortion-free solid-fluid interface rather than through the undulating, refracting fluid-air interface. The IDTs, with 25 finger pairs and a wavelength (see λ_{SAW} in Fig. 2) of 200 μms, operate with a resonant frequency of 19.37 MHz. The electrical signal was supplied at this frequency using an RF signal generator (Agilent N9310A) and RF power amplifier (Amplifier Research 10W1000C). The applied power was limited to 250 mW in order to achieve the desired acoustic streaming whilst avoiding the onset of drop translation or atomization. Except for the circular region shown in Fig. 4, the surface of the SAW device was coated with strongly

hydrophobic Teflon AF (601S1-100-6, DuPont, USA) to aid in constraining the drop from translating during irradiation by the SAW. A 30 μl water drop was used throughout to study the flow field developed as a result of the SAW-fluid interaction. Here the drop position is offset from the centerline of the SAW propagation pathway to provide asymmetric SAW radiation, as shown in Fig. 4.

In order to obtain velocity data of the flow field within the bulk whilst being actuated upon by SAWs, a microPIV study was carried out. Such a study evaluates the velocity vectors of a plane flow field by tracking the motion of particles in the field of view over a set time interval, with the assumption that the chosen particles are too small to have either any significant effect on the flow field or significant inertia. Particles that meet these criteria are simply dragged along with the flow with behavior similar to the local flow field; here 5 μm fluorescent melamine particles (76327-Fluka, Sigma-Aldrich, Missouri USA) at a concentration of 10^8 particles/ml were chosen. Assuming a mean streaming velocity of 5 mm/s, we calculate the Stokes drag on 5 μm melamine particles to be on the order 10^{-10} N, while models developed by Yosioka and Kawashima (1955) and King (1934) estimate the acoustic radiation force on the particles to be on the order of 10^{-12} N, indicating that local fluctuations in the particle dynamics due to the high frequency acoustic forcing are unimportant. The particle trajectories are therefore enslaved to the flow field, and hence the suitability of the microPIV technique to capture the dynamics of the flow field. An inverted fluorescence microscope (IX71, Olympus, Tokyo, Japan) connected to a 1344 × 1024 CCD camera (Hisense MKII, Dantec Dynamics, Skovlunde, Denmark) provided images of the fluorescent particles illuminated with a synchronised, pulsed 532 nm Nd:YAG

Fig. 3 Various symmetry-breaking configurations used to generate asymmetrical SAW radiation into a drop. (**a**) Absorbing gel placed on part of the reflector IDT to partially absorb the SAW reflection. (**b**) Diagonal cut of the SAW substrate edge to induced asymmetric reflection of the SAW. (**c**) Asymmetric positioning of the drop such that only part of the drop lies in the SAW transmission pathway

Fig. 4 The SAW device used in the particle concentration experiments

laser (New Wave Research, CA, USA), all controlled by FlowMap (Dantec Dynamics, Skovlunde, Denmark), a two-dimensional particle tracking software. The same software was also used to compute the in-plane velocity vectors at equally spaced grid points within the flow field.

Since the microPIV technique only provides two-dimensional, planar velocity vector data defined by the focal plane of the imaging camera, a series of planar cross-section 'confocal' slice microPIV measurements were made at discrete layers with intervals of 200 μm through the depth of the drop. Each layer was approximately 20 μm thick. To achieve this, a UPlanFL N 4X 0.13 PhP (Olympus, Tokyo, Japan) objective on the microscope was carefully adjusted using a motorized microscope stage (ProScan II, Prior Scientific, Cambridge, England) to focus on the desired plane—with this objective, a 5 mm × 6.75 mm field of view was obtained. A 100 ms time interval was imposed while acquiring an image pair for the microPIV measurements at each focal plane. The resulting dataset represents the fluid velocities within an entire cross-sectional plane across the diameter of the drop. Figure 5 provides an illustration of the microPIV setup, the outputs of which are the computed U (in the x direction) and V (in the y direction) velocity vectors, as shown in the figure. This data has been measured from 200 to 1,400 μm above

the substrate surface, representing a large portion of the drop volume.

We note that given a hydrodynamic timescale of $L/U \sim \mu L/\gamma \approx 10^{-4}$ s, wherein L and U are the characteristic length and velocity scales of the flow, and μ and γ are the viscosity and surface tension, respectively, the flow equilibrates within milliseconds. To ensure that the flow is steady, data acquisition with the microPIV was initiated 2 s after fluid actuation had commenced. Since particle concentration occurred close to the substrate surface, measurements were initiated at the 200 μm plane. This allowed us to acquire the best possible microPIV results by minimizing the presence of clustered particles within the field of view. Data acquisition across the seven layers (200–1,400 μm) was completed within 30 s, well before complete concentration of the particles was achieved.

3 Numerical simulation

Numerical simulation was carried out using the finite element computation fluid dynamics simulation package ANSYS CFX 11.0 (ANSYS Inc., Canonsburg, PA USA). The fluid drop atop the substrate was modeled as a single phase hemispherical viscous domain with a volume of 30.3 μl and a diameter of approximately 2.4 mm. The air-fluid interface was modeled as a rigid shear free boundary while the fluid-substrate interface was modeled to have a no-slip boundary condition to simulate the solid-fluid interaction at the substrate. This allowed us to avoid a sequential coupling algorithm with its concomitant costs to couple the fluid-structure interactions if the piezoelectric substrate and the fluid were to be modeled and solved separately. The assumption that the free surface could be modeled as a rigid free surface was based on the fact that the energy supplied to the fluid (for acoustic streaming) via the SAW in the experiments was far below the amount needed to induce interfacial destabilization or affect drop symmetry. Even at higher power levels than that used in this study, capillary wave undulations found on the surface are extremely small and—curiously—at frequencies measured in kHz, thus having a negligible effect on the flow regime in the bulk (Li et al. 2008). In addition, the Teflon hydrophobic coating constrains the contact lines and to some extent the motion of the drop's free surface.

The domain was created using four-node quadrilateral elements to generate a nonuniform, 504,000 node mesh; the nodal density at the fluid-substrate interface was higher to enable accurate modeling of the short-wavelength SAW. The interaction between the substrate and the fluid was introduced as a boundary condition at this interface by supplying surface velocities to mimic the SAWs on the LN substrate. A scanning Laser Doppler Vibrometer
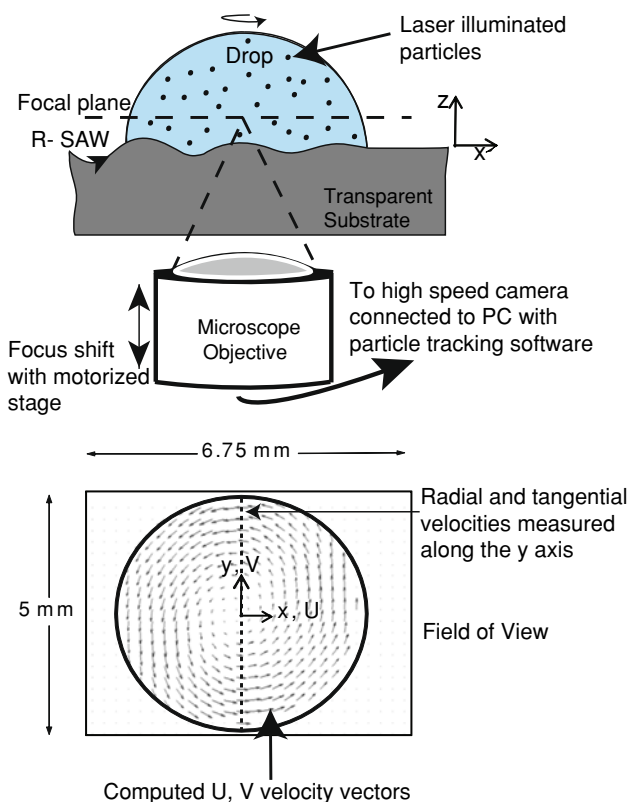
Fig. 5 Confocal microPIV setup employed to visualize the three-dimensional flow field within the drop

(LDV, MSA–400, Polytec PI, Waldbrunn Germany), capable of measuring vibration velocities from a few nm/s to 10 m/s from DC to 40 MHz in frequency, was used to measure the velocity of the substrate surface in a direction perpendicular to the surface; for more information on the working principle of the LDV, the reader is referred to the description in the supplementary information in Li et al. (2008). The circular region shown in Fig. 4 was scanned using the LDV while supplying the IDTs with 250 mW of power to visualize the path and amplitude of the SAW across the contact area of the drop on the substrate. The LDV output shown in Fig. 6 illustrates the results obtained for the out-of-plane surface velocities on the substrate in the absence of the drop. In the figure, the vibration amplitudes are the highest in the cool coloured regions and diminish to zero in the warm regions. As seen, there is a decay in the out-of-plane surface amplitudes and therefore also in the velocities across the width of the drop in the y-direction. The hemispherical domain marked out on the figure corresponds to the position at which the drop is placed on the substrate during the experiments. These surface velocities were measured to have a maximum value of 0.15 m/s at the IDT and were seen to decay exponentially across the SAW propagation direction such that there was negligible motion of the substrate at the center of the drop. To mimic the amplitude and periodic nature of the SAW, the surface velocity data supplied to the simulation was broken down into its components with U, V and W being the velocity of the substrate surface along the x-, y- and z-directions, respectively. The following expressions were supplied as the boundary conditions at the substrate-fluid interface:

$$U = 0.15\sin(-kx + \omega t)\delta_x\delta_y, \tag{1}$$

$$V = 0, \text{ and,} \tag{2}$$

$$W = 0.15\cos(-kx + \omega t)\delta_x\delta_y, \tag{3}$$

where $k = 31733.3$ m^{-1} and $\omega = 126 \times 10^6$ rad/s refer to the wavenumber and the angular frequency of the SAW, respectively. Owing to the optical aberrations caused by the surface curvature of the drop, surface velocities could not be evaluated with the LDV at the fluid-substrate interface with
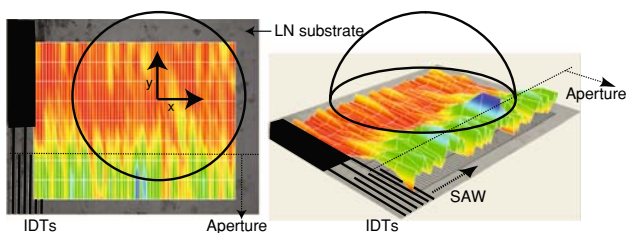
the drop atop it. Hence, in Eqs. 1 and 3, $\delta_x = e^{-(2500x + 6.25)}$ and $\delta_y = e^{-(2500y + 6.25)}$ are functions incorporated to approximate the decay of SAW amplitudes such that their values diminish to zero within one drop radius from the contact line in the positive x- and y-directions. Mesh motion was incorporated in the CFX model to include surface velocity components normal to the boundary.

The steady-state simulation was run while incorporating the *total energy model* wherein the transport of enthalpy is modeled with the inclusion of kinetic energy effects. This model allowed for compressibility and viscous energy dissipation through the medium to be taken into account. A coupled multi-grid control-volume-based solver was used to discretize and solve the steady, compressible continuity and Navier-Stokes equations,

$$\nabla \cdot (\rho\mathbf{u}) = 0, \tag{4}$$

and

$$\rho(\mathbf{u} \cdot \nabla)\mathbf{u} = -\nabla p + \left(\mu_b + \frac{4}{3}\mu\right)\nabla(\nabla \cdot \mathbf{u})$$
$$- \mu\nabla \times (\nabla \times \mathbf{u}), \tag{5}$$

where $\mathbf{u} = (u, v, w), \rho, p, \mu$ and μ_b represent the velocity field, fluid density, fluid pressure, shear viscosity, and bulk viscosity, respectively. The multi-grid based approach employed allowed for accurate calculations of long wavelength effects while the coupled aspect of the solver handled local effects (ANSYS CFX-Solver Theory Guide 2006). This dual approach allows the solver to generate successively coarser grids which enables the solution information to propagate rapidly across the domain thereby reducing computational cost and time whilst also ensuring volume conservation over larger control volumes. Simulations were run until convergence was obtained with the momentum and mass residuals falling to a value below 10^{-5}.

Laminar flow was assumed in the model due to the low Reynolds number of the flow associated with the setup. Fluid properties of water were used while solving the compressible Navier-Stokes equation with the fluid density being calculated based on the pressure using the ideal gas equation. In previous work on acoustic streaming by Sankaranarayanan et al. (2008), Loh et al. (2002) and Nyborg (1965) the fluid has been treated as an incompressible medium with numerical simulation results in the former two studies corroborating well with those from experiments. In this study however, no significant variation in the results was observed upon treating the fluid as either a compressible or an incompressible medium. We believe that this is because in the long time-averaged flow, compressibility effects are localized within a thin boundary layer of thickness $\sqrt{\mu/\rho\omega}$, typically submicron, adjacent to the substrate (Qi et al. 2008).

Fig. 6 LDV measurements of the out-of-plane substrate velocities showing the decay in the y-direction across the drop. The wavy patterns emerging from the IDTs are the SAWs that propagate along the substrate through the fluid-substrate interface

4 Results and discussions

4.1 Experimental observations

Figures 7 and 8 illustrate data obtained, respectively, from the microPIV and numerical simulation, depicting the variation in azimuthal velocities in the drop along discrete planes through its height. The results show similar qualitative trends wherein the azimuthal velocities generated in the fluid increase both with height in the drop and radial distance from the center. The profile is obtained by measuring the tangential velocities along the y-axis (dashed line in the vector field shown in Fig. 5) across the width of the drop in each of the planes. These velocities are in good agreement with the analytical expression for the acoustic streaming velocity given in Rife et al. (2000),

$$u_{as} = \frac{PR^2}{7.11Ac\mu l}, \tag{6}$$

where P is the applied power, R the drop radius, A the irradiation area through which the acoustic energy is transmitted into the drop, c the sound speed in water, and l the acoustic absorption length, which is typically between 10^{-3} and 10^{-2} m/s for values of the parameters corresponding to the experimental setup. The discrepancy in the experimental and numerical velocities can be attributed to approximations invoked in supplying the SAW as a boundary condition in the model. The SAW velocity decay profile at the fluid-solid interface had to be approximated as the surface curvature of the drop caused diffraction of the laser beam, hampering the LDV measurements of the substrate vibration velocity underneath the drop. Nevertheless, the reasonable agreement between the numerical velocity profiles and the analytically verified experimental velocity profiles at least inspires some confidence that the numerical model captures sufficient physics in order to provide a qualitative picture of the SAW-driven complex fluid flow.

The fluid within the bulk rotates in a fashion similar to a forced vortex or rigid body where the azimuthal velocity of the fluid scales linearly with the radius and decays to zero at the vortex center. The figures show slightly larger velocities in the left half of both the graphs as this region of fluid is closest to the SAW radiation path. Figure 9 illustrates the interaction of the fluid and the SAW close to the substrate. In the figure, the darker arrows represent regions of faster moving fluid within the domain. It is seen that the fluid in the vicinity of the SAW irradiated region of the drop footprint is thrust diagonally upwards at an angle commensurate with the Rayleigh angle (see Fig. 2). The fluid is then forced to circulate halfway around the drop only to descend towards the substrate along the opposite side. Thus bulk flow ensues as a result of the leakage of the SAW energy into the drop at the interface; this energy
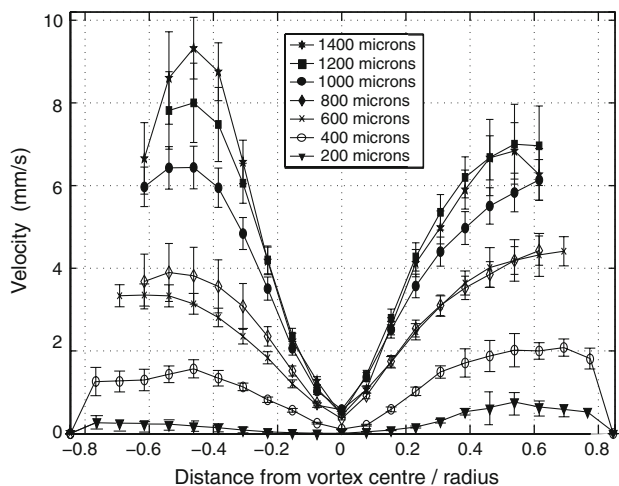

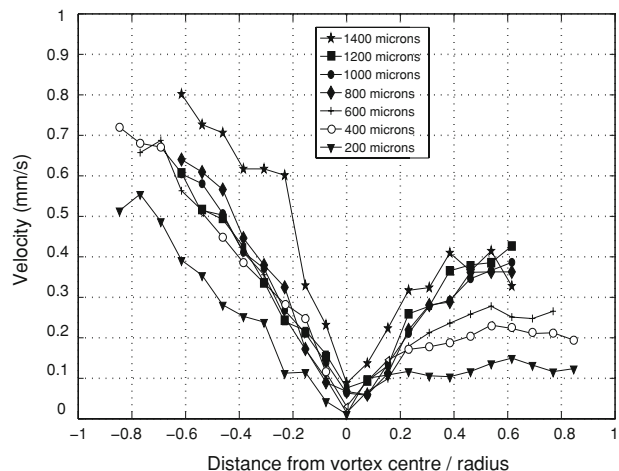**Fig. 7** In-plane velocities across the height of the drop obtained from experiments

Fig. 8 In-plane velocities across the height of the drop obtained from numerical simulations
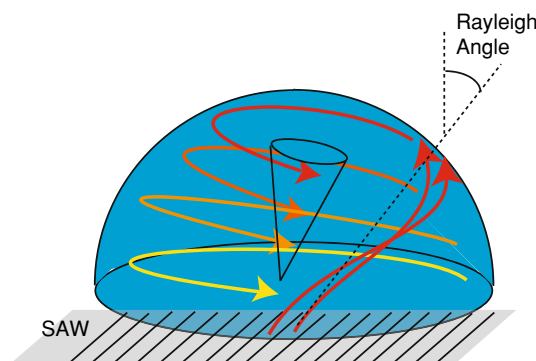

Fig. 9 Schematic illustrating the fluid-SAW interaction leading to the azimuthal velocities observed

however decays in the direction of SAW propagation. As the fluid travels around the drop it loses velocity, as seen by the dip in the velocity values in the right half of the Figs. 7 and 8, only to be driven faster, once again, when it re-enters the region exposed to the SAW.

In-plane radial velocities evaluated from the microPIV results are illustrated in Fig. 10. The data represents the velocities measured at each plane along the y-axis (dashed line in the vector field shown in Fig. 5) across a line passing through the center of the vortex. Hence, a positive radial velocity in the left half of the figure indicates a velocity vector pointing inwards and a positive velocity value in the right half of the figure indicates a radial velocity directed outwards. In Fig. 10, the dashed line is a representation of what such a profile would look like if the flow field was perfectly solenoidal. From the results it is evident that in the lower regions of the drop, there is a net inwards radial velocity which gradually disappears at about 800–1000 μm above the substrate where nearly solenoidal flow is established. In measurements made at heights above this value, there is evidence of a radial velocity directed outwards implying the existence of secondary flow recirculation up the central vortex column. Similar secondary meridional flow recirculations structures were first observed in Yeo et al. (2006a) and Arifin et al. (2007).

Figure 11 provides a graphical representation of the vortex shape established within the drop. The plot is generated by tracing a fixed (but arbitrary) stream function value at each measurement layer across the height of the drop. The inverted cone illustrated by the dashed lines provides further confirmation of the postulated upward secondary recirculation through the central vortex column.
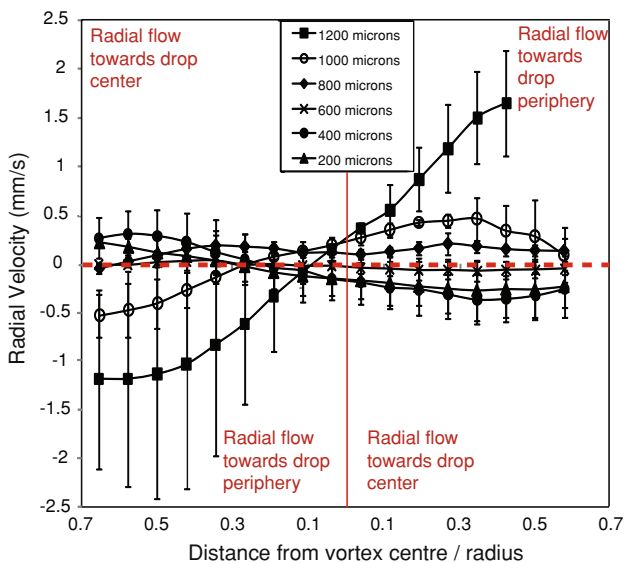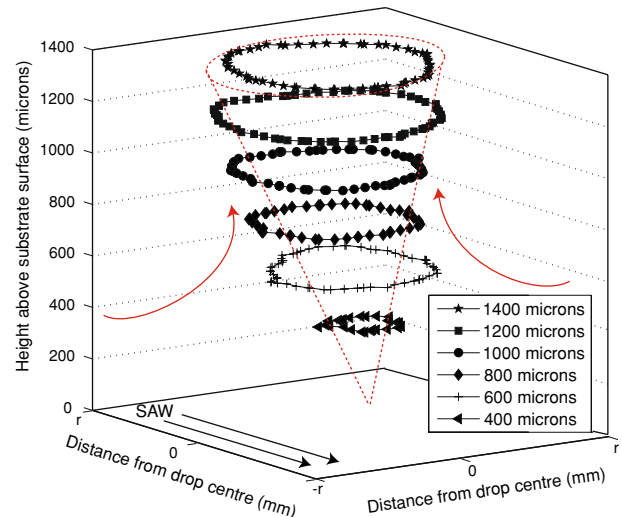
Fig. 11 Shape of the vortex evaluated by tracing a fixed (but arbitrary) stream function value across the height of the drop

From the figure, it can be seen that the vortex is tilted towards the direction of the SAW at a small angle. This angle of inclination proved quite difficult to measure in the experiments owing to the drop free surface curvature. Applying fluid continuity,

$$w = \left(\frac{\delta u}{\delta x} + \frac{\delta v}{\delta y}\right)(z_1 - z_2) + f(x, y), \qquad (7)$$

the individual two-dimensional data sets measured in the planar confocal cross-section at the various drop heights can be employed to calculate the vertical velocities, which then allow a reconstruction of the three-dimensional flow field (Pommer et al. 2007).

In Eq. 7, $(z_1 - z_2)$ refers to the distance between the planes of integration and $f(x,y)$ is an arbitrary function of integration, which requires prior knowledge of the boundary conditions or a plane of symmetry. In our case, the zero velocity no-slip condition was used at the substrate-fluid interface to calculate the out-of-plane velocity components. Once integrated to find the out-of-plane velocity components at each of the seven measurement planes, a smoothing function was used on the data. Using this three-dimensional flow field, streamlines originating from the 400, 600, 1,000 and 1,200 μm planes have been computed and displayed in Fig. 12. The arrows indicate the net direction of flow observed along these streamlines. As described earlier, the results obtained from the out-of-plane velocities show a distinct secondary flow pattern with fluid from the region close to the substrate rising through the central vortex column through to a height of approximately 900 μm. At heights above this plane, the flow field is predominantly solenoidal with very weak secondary flow. In Fig. 12d, streamlines from the outer periphery move towards the substrate albeit with a very small vertical


Fig. 10 In-plane radial velocities across the height of the drop obtained from experiments
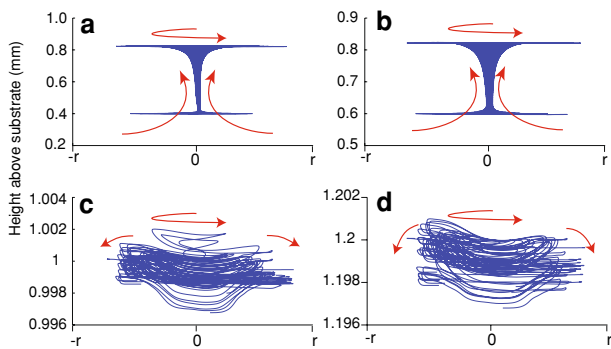
Fig. 12 Streamlines generated from the three-dimensional velocity field at different planes through the drop height: (a) 400 μm, (b) 600 μm, (c) 1000 μm and (d) 1200 μm

Fig. 13 Streamlines originating from the free surface of the drop illustrating the three dimensional flow field obtained from the numerical simulation. The striped pattern in (a) indicates the SAW on the fluid-solid interface

component directed to the bottom. This can be attributed to flow continuity within the domain which would require the fluid near the free surface to be driven towards the substrate while the fluid in the center of the domain spirals upwards, as depicted by the sketch in Fig. 11.

Figure 13 provides a graphical depiction of the flow field evaluated through the numerical simulation. In the figure, the lines represent streamlines of the flow originating from equally spaced grid points at the free surface of the drop. The arrows, on the other hand, indicate the net flow of the fluid as determined from the streamlines. These results also indicate a secondary recirculation up the central vortex column in addition to the azimuthal fluid circulation. In addition, the figure shows the region of the fluid-substrate interface that is subjected to the SAW radiation during the simulations. Similar to what was observed in the experimental results in Fig. 11, albeit to a smaller extent, the streamlines show the central vortex to be tilted towards the region of the drop close to the substrate, subject to the leakage of the SAW radiation from the substrate. During the experiments (not shown), the angle of tilt was noted to become more pronounced as the applied power was increased. The curvature of the streamlines in Fig. 13, particularly in the central column decreases with height through the drop suggesting the presence of the inverted cone-shaped vortex as observed in Fig. 11. Another important observation, as illustrated in Fig. 9 is that the fluid at the substrate surface directly above the SAW radiation path is forced upwards and diagonally from the substrate at the Rayleigh angle θ_R. This feature of the flow field is also clearly seen in Fig. 14 which provides an illustration of the three-dimensional velocity vectors measured on two-dimensional cross-section planes at various heights of the drop obtained using the microPIV technique. As observed in Figs. 13 and 14, fluid approaching the region directly above the SAW irradiation is first driven downwards due to the negative pressure before being thrust upwards diagonally along the Rayleigh angle into the
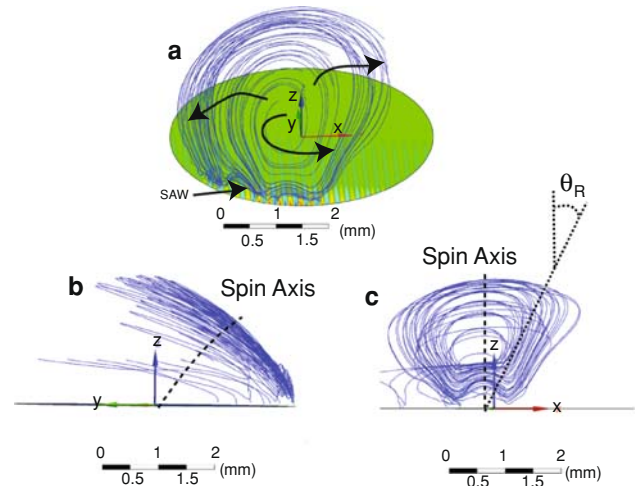
higher regions of the drop once it is directly above the irradiation. The reducing vertical component of the velocity vectors moving into the higher regions of the drop also illustrates the fluid streaming to decrease in magnitude through the height of the drop. In addition, these plots also illustrate the existence of the suggested secondary meridional flow through the central vortex column, particularly in the lower regions of the drop.

4.2 Physical mechanism

The experimental and numerically computed three-dimensional flow characteristics bear striking resemblance to Batchelor flows (Batchelor 1951) occurring in a cylindrical fluid column trapped between a rotating disk on top and a stationary one at the bottom (Pao 1972; Yeo et al. 2006a; Arifin et al. 2007). The fluid-solid interface through which the SAW interacts with the drop can be regarded as a no-slip boundary (akin to the bottom stationary disk in the example above), due to the fact that the SAW radiates through only a small area of the contact footprint of the drop. Due to the constraints induced by the drop size and capillarity, volume conservation requires the fluid actuated by the induced long-range (Eckart) streaming to recirculate in a circumferential manner, as depicted in Fig. 15. As such, the fluid layer close to the top free surface of the drop—where the azimuthal velocity is the largest—resembles the top rotating disk in the Batchelor flow problem.

In Batchelor flows, the azimuthal recirculation of the fluid induces a secondary meridional circulation due to which the fluid flowing down the side walls recirculates back up through a central column. This is consistent with

Fig. 14 Three-dimensional velocity vector plot illustrating the flow field measured at different planes through the drop height: (**a**) 1400 μm, (**b**) 1000 μm, (**c**) 600 μm and (**d**) 200 μm
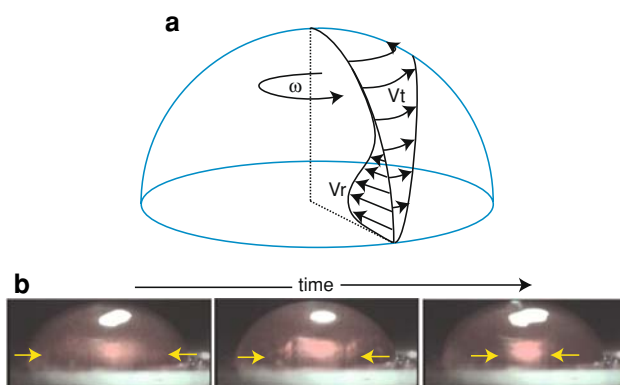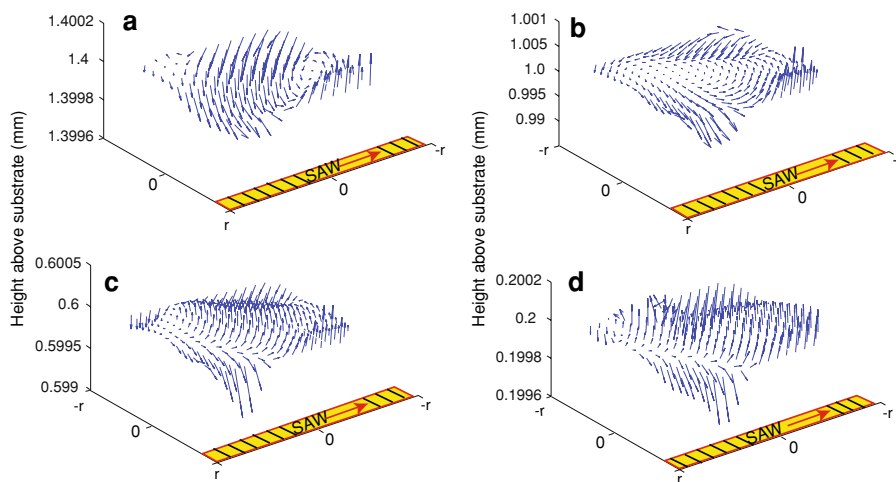

Fig. 15 (**a**) Schematic illustration of the three-dimensional flow field developed within the bulk. (**b**) Experimental images supporting the existence of the flow field illustrated

the observations made in our numerical and experimental results in Figs. 10, 12 and 13. This occurs due to an inward radial velocity that appears in the Ekman layer close to the friction surface at the fluid-substrate interface (Benton and Clark 1974). Since the centrifugal force scales as the square of the azimuthal velocity, it diminishes close to the substrate surface (see Figs. 7, 8, 15a) due to the no-slip condition, thus promoting a net inward motion in this region.

Figure 16 provides further evidence to support the postulated mechanism. Figures 16b–d are time lapsed frames extracted from video capture at 60 frames/s which depict a cluster of particles rising through the central vortex column over a period of time. Particles seeded in the flow field are then transported with the fluid circumferentially in a spiral-like manner around the drop periphery toward the bottom regions of the drop, as illustrated in Fig. 9. Once they reach the Ekman layer, the particles are pushed along the substrate into the center of the drop due to the inward radial flow in this boundary layer (Fig. 15a, b) and appear to cluster there. We note that due to volume conservation,

the fluid does not terminate at a bottom stagnation point at the apex of the inverted cone sketched in Fig. 15a but recirculates back up along the central column through the cone. However, the particles appear to stack into a conical heap as shown in the inset of Fig. 16a. This can be explained by decomposing the apparent particle velocity into the sum of the fluid velocity **u** and the true particle velocity **v** (Arifin et al. 2007). Whilst particle trapping at the stagnation point requires their trajectories to converge onto a single point where **u** = 0, this is clearly impermissible given flow continuity as alluded to earlier. Nevertheless, particles can still be trapped at a stagnation point, as observed in Fig. 16, if **u** is sufficiently small, typically true near fixed points. If the particles suffer from a local force, supplied by the sedimentation force in our case, and if there is insufficient convective fluid velocity in these regions to overcome such forces, then **v** can essentially act in the opposite direction of **u**, thus converting **u** into an attractor. Therefore at low applied powers when the convection near the fixed point is weak, we observe the particles to be trapped in a conical heap in a central position on the substrate, as shown in Fig. 16. Such three-dimensional images of the SAW particle concentration process are observed for the first time here, as compared to the two-dimensional planar images of the particle concentration in Li et al. (2007) and Shilton et al. (2008). In any case, the particle concentration dynamics in Fig. 16 provide support for the Batchelor flow analogy postulated above, in particular, the existence of the meridional flow currents and the Ekman boundary layer.

Occasionally, a few particles are observed to escape from the stagnation node and travel back up through the central column of the drop, as highlighted by the circled regions in Figs. 16b–d. This is consistent with the resuspension and redispersion of the particles above a threshold value of the applied power in Li et al. (2007). Given that the sedimentation force acting on the particle scales as a^3
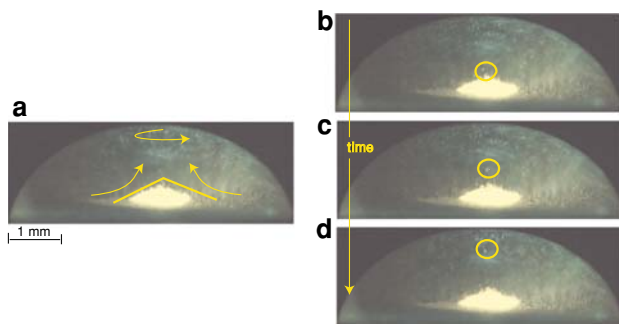
Fig. 16 Experimental images acquired at 60 frames/s illustrating the trapping of fluorescent particles into a conical stack on the substrate at a central location at the bottom of the drop. Image **a** illustrates the effect of the Ekman layer in establishing the meridional flow which leads to the conical heap of particles in the centre. Occasionally there is sufficient convection to force just a few particles to overcome the sedimentation force and escape form the heap to rise with the fluid back up the central column as shown by the circled regions in the images **b–d**

and the viscous drag on the particle scales as a, $\mathbf{v} \sim a^2$, which suggests that the concentration time scales as $1/a^2$, as observed in Li et al. (2007).

5 Conclusions

For the first time, the three-dimensional flow field of the azimuthal fluid recirculation in a sessile drop arising from asymmetric SAW radiation is revealed through confocal type reconstructions of two-dimensional planar micropraticle image velocimetry experiments and supported through simplified finite element numerical simulations. This is an extension to previous two-dimensional planar flow visualization studies which demonstrated the powerful microcentrifugation effect that could be driven using the SAW for effective micromixing or particle concentration and separation.

Our results shed light on the fundamental mechanism by which the particles collect. Due to the fluid-structural coupling, the SAW is diffracted into the drop at the Rayleigh angle. The longitudinal pressure fronts that arise drive long-range Eckart streaming, also known as acoustic streaming, within the drop. Due to the irradiation leakage at the Rayleigh angle, the primary flow is forced in this direction. However, due to the deliberate asymmetry of the SAW radiation on the drop and the confinement of the fluid due to capillarity, the fluid recirculates azimuthally, around the top of the drop, in a similar manner to the azimuthal recirculation imposed by a top rotating disk in Batchelor flows; the no-slip condition of the substrate on which the drop sits resembles the second stationary disk in the Batchelor flow description. Fluid therefore recirculates

downward in a spiral-like manner around the periphery of the drop.

Particles suspended in the flow field therefore follow the fluid trajectory and are convected in a spiral-like manner akin to an inverted cone structure to the bottom region of the drop. However, due to the inward radial velocity in a thin boundary layer adjacent to the substrate, known as the Ekman layer, the particles together with the fluid are then forced inwards radially once they enter this boundary layer region. The fluid recirculates back up a central column in the middle of the drop due to flow conservation but the particles are trapped and stack into a heap at a central stagnation point at the bottom if the convective forces are insufficient to overcome the sedimentation forces acting on the particle.

If, however, the convection is sufficiently strong, for example, by increasing the applied power beyond a threshold value, these particles escape from the agglomerate and are redispersed in the bulk, consistent with previous two-dimensional observations. The true velocity of the particle scales as the square of the particle size, again consistent with previous observations in which the particle concentration time is seen to scale as the inverse of the particle dimension squared. This three-dimensional picture therefore provides helpful insight for practical methods to control and optimize this technique. These findings can help expedite the development of microfluidic particle concentration and separation devices for which there is currently a dire need; for example, in applications involving the separation of blood plasma from red blood cells as a necessary precursor step in point-of-care medical diagnostic devices and for the concentration of pathogens in miniaturized biosensors.

References

Alvarez M, Friend JR, Yeo LY (2008a) Rapid generation of protein aerosols and nanoparticles via surface acoustic wave atomization. Nanotechnology 19:455103

Alvarez M, Friend JR, Yeo LY (2008b) Surface vibration induced spatial ordering of periodic polymer patterns on a substrate. Langmuir 24:10629–10632

Alvarez M, Yeo LY, Friend JR (2009) Rapid production of protein loaded biodegradable microparticles using surface acoustic waves. Biomicrofluidics 3:014102

ANSYS CFX-Solver Theory Guide (2006) ANSYS, Inc., p 294

Arifin DR, Yeo LY, Friend JR (2007) Microfludic blood plasma separation via bulk electrohydrodynamic flows. Biomicrofluidics 1:014103

Batchelor GK (1951) Note on a class of solution of the navier-stokes equations representing steady rotationally symmetric flow. Q J Mech Appl Math 4:29–41

Benton ER, Clark A (1974) Spin up. Annu Rev Fluid Mech 6:257–280

Blattert C, Jurisekha R, Tahhan I, Schoth A, Kerth P, Menz K (2004) Separation of blood in microchannel bends. In: Proceedings of the 26th annual international conference of the IEEE. Engineering in Medicine and Biology Society, San Francisco

Brody JP, Osborn TD, Forster FK, Yager P (1996) A planar microfabricated fluid filter. Sens Act A 54:704–708

Ducree J (2008) Centrifugal microfluidics. In: Li D (ed) Encyclopedia of microfluidics and nanofluidics. Springer, New York

Friend J, Yeo L, Arifin D, Mechler A (2008) Evaporative self-assembly assisted synthesis of polymer nanoparticles by surface acoustic wave atomization. Nanotechnology 19:145301

Hodgson RP, Tan M, Yeo L, Friend J (2009) Transmitting high power rf acoustic radiation via fluid couplants into superstrates for microfluidics. Appl Phys Lett 94(2):024102

King L (1934) On the acoustic radiation pressure on spheres. Proc R Soc Lond A 147:212–240

Li H, Friend JR, Yeo LY (2007) Surface acoustic wave concentration of particle and bioparticle suspensions. Biomed Microdev 9:647–656

Li H, Friend JR, Yeo LY (2008) Microfluidic colloidal island formation and erasure induced by surface acoustic wave radiation. Phys Rev Lett 101:084502

Loh B-G, Hyun S, Ro PI, Kleinstreuer C (2002) Acoustic streaming induced by ultrasonic flexural vibrations and associated enhancement of convective heat transfer. J Acoust Soc Am 111:875–883

Madou M, Kellogg G (1998) LabCD: a centrifuge-based platform for diagnostics. In: Proceedings of the SPIE, vol 3259, pp 80–93

Meng AH, Wang AW, White RM (1999) Ultrasonic sample concentration for microfluidic systems. In: Proceedings of the tenth international conference on solid-state sensors and actuators, pp 876–879

Nyborg WL (1965) Physical acoustics, vol 2B. Academic Press, New York

Pao H-P (1972) Numerical solution of the navier-stokes equations for flows in the disk-cylinder system. Phys Fluids 15:4

Papautsky I, Asgar A, Bhagat S (2008) Microscale flow visualization. In: Li D (ed) Encyclopedia of microfluidics and nanofluidics. Springer, New York

Pommer MS, Kielhl AR, Soni G, Dakessian NS, Meinhart CD (2007) A 3d–3c micro-piv method. In: Proceedings of the second IEEE international conference on nano/micro engineered and molecular systems, p 074103

Qi A, Yeo LY, Friend JR (2008) Interfacial destabilization and atomization driven by surface acoustic waves. Phys Fluids 20:074103

Rife J, Bell M, Horwitz J, Kabler M, Auyeung R, Kim W (2000) Miniature valveless ultrasonic pumps and mixers. Sens Actuators 86:135–140

Sankaranarayanan SKRS, Cular S, Bhethanabotla VR, Joseph B (2008) Flow induced by acoustic streaming on surface-acoustic-wave devices and its application in biofouling removal: a computational study and comparisons to experiment. Phys Rev E 77:066308

Sengupta S, Chang H-C (2008) Microfilters. In:Li D (ed) Encyclopedia of microfluidics and nanofluidics. Springer, New York

Shilton R, Tan MK, Yeo LY, Friend JR (2008) Particle concentration and mixing in microdrops driven by focused surface acoustic waves. J Appl Phys 104:014910

Tan MK, Friend JR, Yeo LY (2007a) Direct visualization of surface acoustic waves along substrates using smoke particles. Appl Phys Lett 91:224101

Tan MK, Yeo LY, Friend JR (2007b) Microparticle collection and concentration via a miniature surface acoustic wave device. Lab Chip 7:618–625

Tan MK, Friend JR, Yeo LY (2009) Anomalous interfacial jetting phenomena induced by focused surface vibrations. Phys Rev Lett (submitted)

Walker GM, Beebe DJ (2002) A passive pumping method for microfluidic devices. Lab Chip 2:131–134

White R, Voltmer F (1965) Direct piezoelectric coupling to surface elastic waves. Appl Phys Lett 7:314–316

Whitesides G (2006) The origins and the future of microfluidics. Nature 442:368–373

Wilding P, Pfahler J, Bau HH, Zemel JN, Kricka LJ (1994) Manipulation and flow of biological fluids in straight channels micromachined in silicon. Clin Chem 40:43–47

Wixforth A (2003) Acoustically driven planar microfluidics. Superlattice Microst 33:389–396

Wixforth A, Strobl C, Gauer C, Toegl A, Scriba J, Guttenberg Z (1990) Acoustic manipulation of small droplets. Anal Bioanal Chem 319:982–991

Yeo LY, Friend JR (2009) Ultrafast microfluidics using surface acoustic waves. Biomicrofluidics 3:012002

Yeo LY, Friend JR, Arifin DR (2006a) Electric tempest in a teacup: the tea leaf analogy to microfluidic blood plasma separation. Appl Phys Lett 89:103516

Yeo LY, Hou D, Maheshswari S, Chang H-C (2006b) Electrohydrodynamic surface micro-vortices for mixing and particle trapping. Appl Phys Lett 88:233512

Yosioka K, Kawashima Y (1955) Acoustic radiation pressure on a compressible sphere. Acustica 5:167–173

Yuen PK, Kricka LJ, Fortina P, Panaro NL, Sakazume T, Wilding P (2001) Micro-fluidics module for blood sample preparation and nucleic acid amplification reaction. Genome Res 11:405